Meas. Sci. Technol. **22** (2011) 085402 (15pp) doi:10.1088/0957-0233/22/8/085402

Measurements of multiple mole fraction fields in a turbulent jet by simultaneous planar laser-induced fluorescence and planar Rayleigh scattering

Cody J Brownell[1] **and Lester K Su**[2]

[1] Mechanical Engineering Department, US Naval Academy, 590 Holloway Rd, Annapolis, MD 21402, USA
[2] Applied Fluid Imaging Laboratory, Department of Mechanical Engineering, The Johns Hopkins University, 3400 N Charles St, Baltimore, MD 21218, USA

E-mail: brownell@usna.edu

Received 27 April 2011, in final form 23 May 2011
Published 20 June 2011
Online at stacks.iop.org/MST/22/085402

Abstract
This paper presents two-dimensional measurements of all individual mole fractions in a three-species, non-reacting turbulent flow, using planar laser-induced fluorescence (PLIF) and planar laser Rayleigh scattering. The flow is an axisymmetric jet of acetone and helium in an air coflow. PLIF measures the acetone mole fraction, while Rayleigh scattering measures a linear combination of the acetone and helium mole fractions. The simultaneous implementation of these techniques allows for the calculation of the helium and air mole fraction fields. The results of this diagnostic method are being used for the study of multicomponent molecular transport effects in turbulent fluid mixing.

Keywords: planar laser imaging, turbulent mixing, multi-species mixing, differential diffusion, Rayleigh scattering, laser-induced fluorescence

1. Introduction

Molecular mixing of chemical species plays a key role in many practical engineering flow systems. In non-premixed reacting flows, for example, mixing of fuel and oxidizer is necessary for chemical reaction. A detailed understanding of mixing is needed for the development of accurate computer simulations of such flows. One aspect of mixing that is particularly ill-understood is the role of variations in molecular transport properties, such as mass diffusivity, among multiple species. While realistic reaction systems involve tens of chemical species, combustion simulations typically represent the full mixing process using a single scalar variable; this so-called mixture fraction, defined as the fraction of mass of local material originating in the fuel stream, is handled using an evolution equation involving only a single mass diffusivity. It is unclear whether such a representation can accurately represent the mixing of multiple species with disparate diffusivities.

The simplest non-reacting mixing system in which the effects of disparate mass diffusivity would appear involves three distinct species (a two-species system can be described by a single interdiffusion coefficient). Consider a jet, with two initially mixed species, issuing into an ambient region containing a third species. Differences in diffusivity would potentially cause the two jet species to mix differentially into the ambient fluid. Experimental investigation of mixing in such a flow requires simultaneous measurement of the concentrations of each jet species. Quantitative planar measurements of single species concentrations in gas-phase flows, which are more relevant to combustion than liquid-phase flows, have been reported using Rayleigh scattering [1–4] and planar laser-induced fluorescence (PLIF) [5–7]. However, extending either method to multiple species concentrations is not straightforward; Rayleigh scattering is not species-specific, while the emission spectra for tracers readily used for PLIF (such as acetone or biacetyl) are not easily discriminated to identify individual tracer concentrations

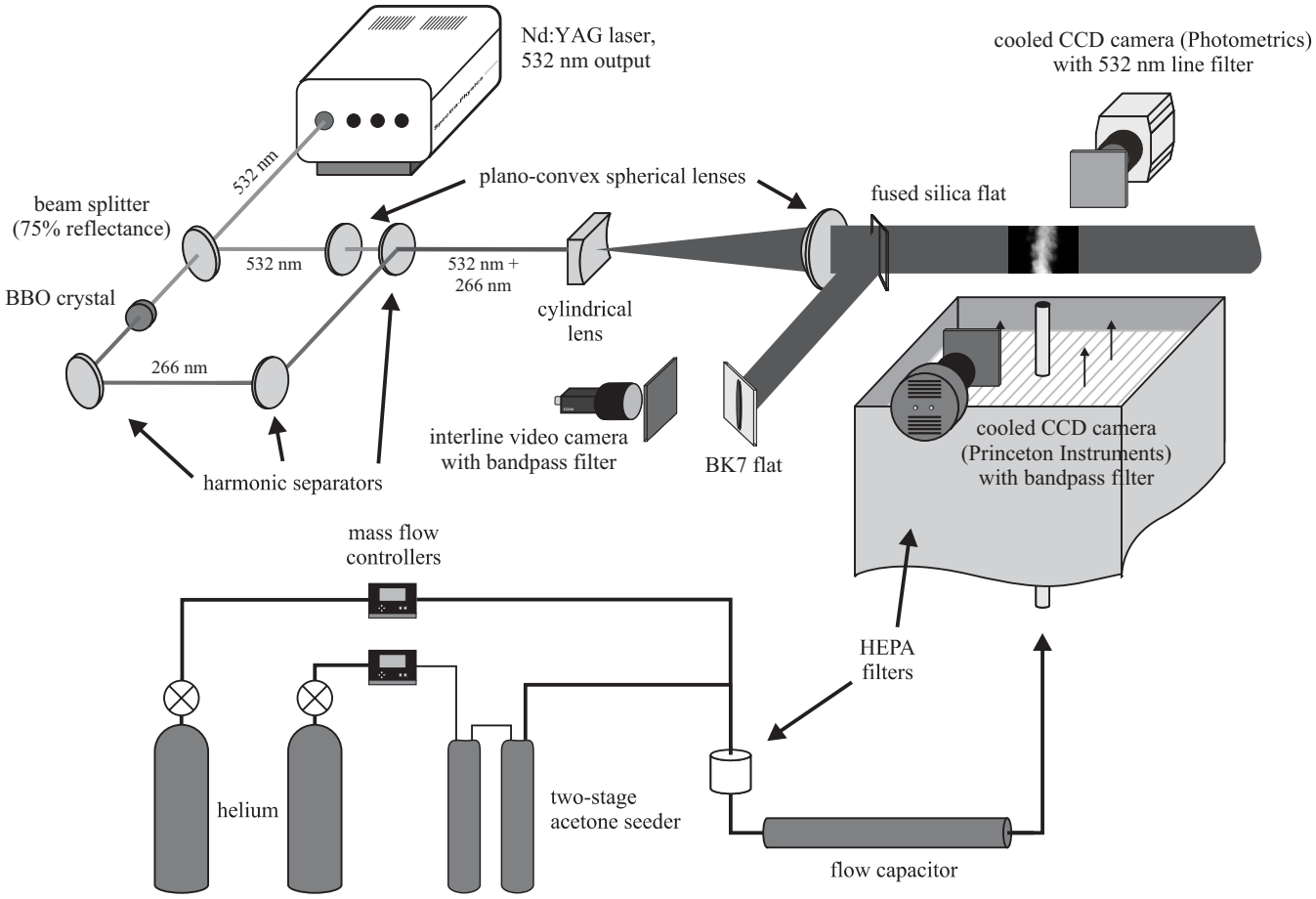

Figure 1. The jet flow facility and imaging arrangement. The imaging experiments employ one laser light source, which generates both 532 nm and 266 nm light sheets, and three cameras. One camera captures the Rayleigh scattering signal, another measures the acetone fluorescence intensity, and the last measures the 266 nm laser sheet intensity distribution.

[8]. Dual-wavelength PLIF can yield simultaneous acetone mole fractions and temperature [9], but, for the temperature differences required for quantitative imaging, temperature is not a passive scalar and does not truly quantify molecular mixing. Similarly, multi-scalar imaging measurements of mixture fraction, temperature and reaction rates in reacting flows [10, 11] do not directly address the underlying multi-species molecular mixing. Previous work in three-species turbulent mixing has measured normalized scalar differences [12–14], but without explicit measurement of individual mole fractions.

In this work, we apply simultaneous PLIF and planar Rayleigh scattering to measurements of multiple species concentrations in a turbulent axisymmetric jet of helium and gaseous acetone issuing into an air co-flow. With only acetone present as a fluorescent marker, PLIF directly measures the acetone mole fraction, X_{ac}. The Rayleigh scattering signal is, when properly corrected for background light levels and spatial variations in laser intensity or image capture, proportional to the local scattering cross-section, which is itself the mole fraction-weighted average of the scattering cross-sections, σ_i, of the constituent species. Here, we employ a normalized signal, Π, which is the scattering signal normalized by the equivalent signal in air only, that is,

$$\Pi = X_{air} + X_{He}\frac{\sigma_{He}}{\sigma_{air}} + X_{ac}\frac{\sigma_{ac}}{\sigma_{air}}. \quad (1)$$

The helium–acetone–air system is advantageous in Rayleigh scattering because the scattering cross-sections differ widely, with the ratios $\sigma_{He} : \sigma_{air} : \sigma_{ac}$ being $0.014 : 1 : 14$ [15], so that Π is sensitive to fluctuations in the individual mole fractions. Using (1) and the definition of the mole fraction, $1 = X_{air} + X_{He} + X_{ac}$, and with X_{ac} known from the PLIF, we can solve for X_{He} and X_{air}. This full knowledge of individual mixture fractions will provide a uniquely comprehensive view of multicomponent turbulent mixing.

2. Flow system

2.1. Flow facility

The experimental arrangement is shown in figure 1. The flow facility is an open, vertical wind tunnel, with a filtered air coflow and a round vertical pipe in the center from which the jet originates. The coflow air is driven by a centrifugal blower through a series of screens and honeycombs, and lastly through a 2 ft × 2 ft, 2 in thick high-efficiency (HEPA) filter, which removes dust and other particulates. Particulates would introduce Mie scattering that would interfere with the detection of the much weaker Rayleigh scattering signal. The coflow

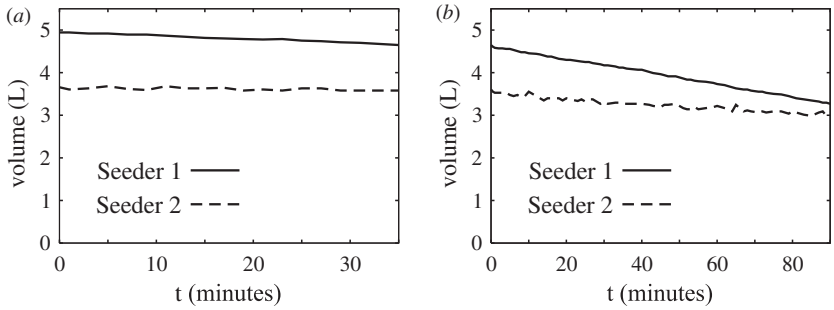

Figure 2. Sample results from tests of the two-stage acetone seeding arrangement, using air as the carrier gas. Each plot shows the liquid acetone volume in each of the two seeder vessels as a function of time for a given experimental run. (*a*) For an air flow rate of 10 SLPM, the mean evaporation rate of acetone liquid is 9.95 mL min^{-1}. (*b*) For an air flow rate of 30 SLPM, the mean evaporation rate of acetone is 27.83 mL min^{-1}. Acetone evaporation rates are essentially constant in time for both flow rates.

velocity 5 cm over the filter was measured to be relatively uniform using a commercial transducer (TSI 8455). The maximum speed, at the center of the facility, is 0.5 m s^{-1}, dropping to no less than 0.3 m s^{-1} within a 25 cm radius.

Despite the use of nominally pure supplies of helium, nitrogen and acetone, contamination in the jet plumbing lines due to dust, corrosion, and other particulates is a problem. Inline filter units for the gas lines, incorporating large cross-sectional area HEPA filters, were purpose-built for these experiments. The filters are effective even after extended exposure to acetone vapor. Inline gas flow rates are measured and regulated by mass flow controllers (Sierra Instruments C-100) that have a rated repeatability of 0.2%. After filtration and measurement, the different jet gases are combined and mixed inside a large pipe (with volume 2.4 L) that serves as a flow capacitor, damping high-frequency oscillations in the composition and flow rate. The jet nozzle is a straight stainless steel pipe, with inner diameter 4.6 mm, length 200 mm, and a machined, square-edged tip.

2.2. Acetone seeding

In quantitative applications of acetone PLIF, details of the acetone seeding method are highly important. Acetone is a liquid at room temperature and must be vaporized for use in flow imaging experiments. This commonly uses a bubbling acetone seeding vessel, in which a carrier gas is introduced at the bottom of a volume of liquid acetone through small holes, forming bubbles that rise through the liquid. The high vapor pressure of acetone, roughly 30% acetone by volume at room temperature (as per the formula given by Ambrose [16]), ensures that it will evaporate rapidly into these bubbles. A mixture of the carrier gas and acetone vapor, in which the acetone is typically assumed to be at or close to its saturation pressure, collects in the closed seeder above the liquid surface, from where it then flows to the jet nozzle.

Measurement and control of the acetone seeding efficiency is particularly challenging with these bubbling systems. The flow rate of acetone vapor is typically determined by measuring the flow rate of the carrier gas, and then estimating the acetone flow rate using the Ambrose formula, given a measurement of the liquid acetone temperature and the assumption of full saturation. However, there is substantial cooling in the seeder caused by the evaporation of the liquid acetone. The acetone vapor pressure is sensitive to temperature, so in the absence of an external heat source, the acetone concentration in the gas outflow will decline noticeably over the course of a given experiment. Even if a heat source is provided for the seeder, it would require non-trivial control of the amount of heat addition to achieve a stable temperature and, thus, a stable acetone seeding efficiency.

In this work, we employ a dual-stage bubbling system, comprising two seeding vessels (each with volume 6.6 L) in series for improved stability and flow rate control. The acetone/carrier gas mixture leaving the first seeder is used as the carrier gas for the second seeder, and the first seeder is equipped with a heating element that allows for user adjustment of heating intensity to reduce the degree of evaporative cooling. The goal of this arrangement is to ensure that the gas issuing from the second seeder is as near as possible to room temperature and contains acetone at the saturation concentration. Without adaptive control of the heating element in the first seeder, excessive heating there will result in acetone concentrations in excess of the room temperature saturation value, in which case the excess acetone will condense from the carrier gas in the second seeder; conversely, if insufficient heating is applied to the first seeder, or if the flow rate is too high to allow for the acetone to reach saturation levels there, the second seeder will introduce the necessary additional acetone to the flow. In either case the rate of condensation or evaporation in the second seeder is small in practice, and the second seeder remains effectively at room temperature, even with no heat source of its own. We can ultimately control the acetone concentration in the jet fluid by combining the gas issuing from the second seeder, in which the acetone is at its saturation pressure, with pure carrier gas in varying proportions.

We performed a series of calibration measurements to determine the steadiness of the acetone seeding with this configuration, as well as its sensitivity to various input parameters (such as acetone liquid level, carrier gas type, carrier gas flow rate, and temperature). Figure 2 shows sample results from direct measurements of the liquid volume in each seeder as a function of time, using air as the carrier gas and

with the air flow rate being held fixed (here, at 10 SLPM and 30 SLPM) over the course of an experiment. For both flow rates, the rate of evaporation in each seeder is effectively constant over the full measurement time, as manifested by the linear behavior of the time dependence of the liquid volume. In the 10 SLPM case (figure 2(*a*)), the measured evaporation rate of liquid acetone is 9.95 mL min^{-1}, corresponding to 32% acetone by volume in the outflow, while in the 30 SLPM case (figure 2(*b*)) the measured acetone evaporation rate is 27.83 mL min^{-1}, corresponding to 30.5% acetone by volume in the outflow. The plots show that essentially all evaporation takes place in the first seeder for the lower flow rate, while for the higher flow rate the first seeder is insufficient to bring acetone to saturation pressure, and some of the evaporation takes place in the second seeder. The temperature in our laboratory (which is not controllable) varied from approximately 24 °C to 27 °C during these experiments, corresponding to saturation acetone volume fractions ranging from 29.0% to 33.2% [16], so we conclude that this seeder configuration is adequate to ensure saturation of the gaseous acetone in the carrier gas flow.

3. Laser diagnostic method

3.1. Laser light source and imaging hardware

The light source used here is a dual-cavity Nd:YAG laser (Spectra-Physics PIV-400), with the two laser cavities being fired simultaneously in these experiments, resulting in an effective laser energy of ≈ 700 mJ per pulse at 532 nm. The laser pulses pass through a sequence of optics that split the beam, further frequency-double 25% of the original energy to 266 nm using a BBO crystal (Inrad), and recollimate the 266 and 532 nm beams. Sheet-forming optics then generate laser sheets with a constant height of approximately 25 mm, and thickness at the focal point (which is typically located directly above the nozzle) of approximately 200 μm. The 266 and 532 nm beams can be made coincident in the cross-sheet direction to within ≈ 20 μm in the measurement region [17]. Cameras oriented perpendicularly to the light sheets, fitted with the appropriate filters, record the Rayleigh scattering and PLIF signals. The cameras used here are thermoelectrically cooled, front-illuminated CCD cameras, a Photometrics CoolSNAP HQ, with 1392 × 1040 pixel resolution, for the Rayleigh scattering, and a Princeton Instruments MicroMAX with 1300×1030 pixel resolution for the PLIF. The Photometrics camera has a quantum efficiency (QE) that exceeds 60% over a range that includes the 532 nm laser wavelength; the QE curve for the Princeton Instruments camera has a slightly lower peak (at 50%) but is weighted more toward the blue side of the visible spectrum, making it well suited for the capture of the acetone fluorescence signal.

3.2. Rayleigh scattering

3.2.1. Rayleigh scattering imaging. Rayleigh scattering is the elastic scattering of light from molecules or particles with a characteristic size much smaller than the light wavelength [18]. The intensity of the scattered light signal is given by $S_{RS} = I N\sigma$, where I is the intensity of the incident laser light, and N and σ are respectively the number density and Rayleigh scattering cross-section of the medium. The scattering cross-section of a given species i, σ_i, relates to its index of refraction, n_i, and the wavelength of the incident light, λ, as $\sigma_i \propto (n_i - 1)^2\lambda^{-4}$, while the scattering cross-section of a mixture of M species is simply the mole fraction-weighted average of the constituent cross-sections or $\sigma_m = \sum_{i=1}^{M} X_i\sigma_i$ [18].

The general form of the normalized scattering signal, Π, for the case of M species is

$$\Pi = \frac{I\,N\,\sigma_m}{I\,N\,\sigma_1} = \frac{\sum_i^M X_i\sigma_i}{\sigma_1}, \tag{2}$$

where the normalizing signal is the scattering signal from a uniform field of species 1. In practice, Π is simply equivalent to the flat-field corrected scattering signal, the measurement of which is described below (section 3.2.2). In a two-component flow system, the normalized signal Π, along with the mole fraction definition $1 = X_1 + X_2$, directly yields both X_1 and X_2. The interpretation of the Rayleigh scattering signal in a flow with three or more species is less straightforward. In particular, the individual X_i cannot be determined directly. An appropriately designed experiment can, nevertheless, yield valuable information regarding the multicomponent mixing. Bilger and Dibble [19] proposed an experiment consisting of a jet with two species mixing into air, where one of the jet species has a refractive index that is greater than that of air, and the other has a refractive index less than that of air. If the initial concentration ratio of the two jet species is specified such that the Rayleigh scattering cross-section of the jet is the same as the scattering cross-section of air, then any local change in the scattering signal is directly indicative of differential diffusion, i.e. a departure of the jet species concentration ratio from its initial value.

In this work, we perform Rayleigh scattering imaging in a three-species flow, consisting of a jet of helium and acetone issuing into air, for which the normalized signal Π is written as (1). The mass diffusivity of helium into air at standard atmospheric conditions is 0.771 cm^2 s^{-1}, while that of acetone vapor into air is 0.104 cm^2 s^{-1}, so differential diffusion may result in significant unmixing of the jet species. Simultaneous PLIF of acetone directly gives information on the acetone mole fraction, X_{ac} (section 3.3). Together with the mole fraction definition, the Rayleigh scattering and PLIF results are sufficient to allow the determination of all three individual mole fractions in the flow.

3.2.2. Data reduction: Rayleigh scattering. In the data reduction process for the Rayleigh scattering images, we first subtract the background light levels to yield the background-corrected signal, S_{RS}; then, we account for non-uniform camera response, laser sheet attenuation, and variations in the instantaneous local laser light intensity, I, across the imaging windows, ultimately yielding the normalized signal Π (2). The low signal levels that characterize Rayleigh scattering experiments place a particular burden of accuracy on the data reduction process. We begin here by implementing

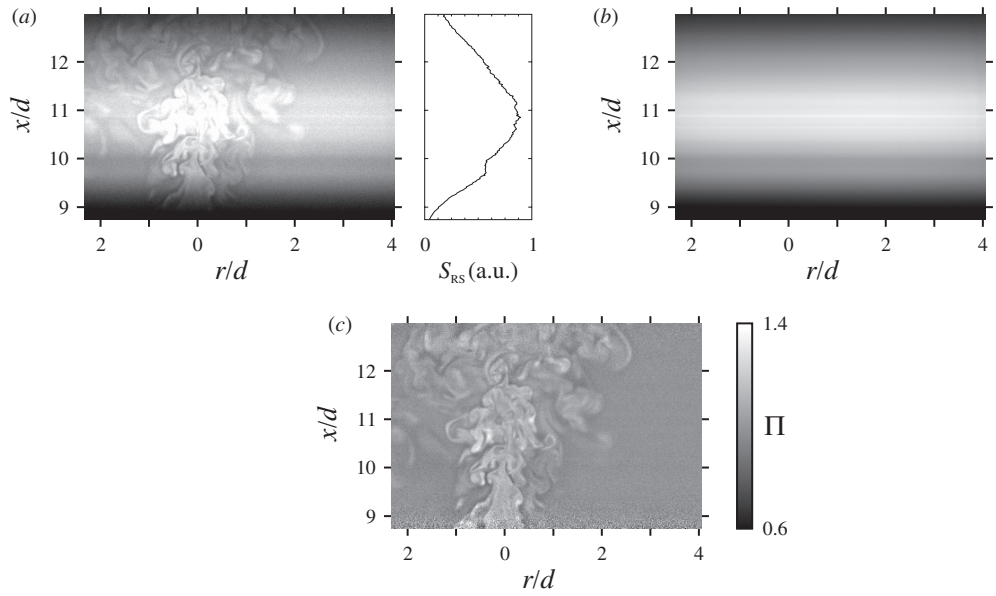

Figure 3. Data reduction for the Rayleigh scattering imaging. (*a*) A sample, background-subtracted scattering image from a jet at $Re_\infty \approx 4600$, together with a cross-sheet intensity profile compiled in the ambient fluid region. (*b*) The averaged background-subtracted scattering image from the same window as in (*a*), but with ambient air in the window only. (*c*) The jet image from (*a*) after further flat-field correction, as described in section 3.2.2.

a novel approach for measuring background light levels. A thorough description of the background measurement is available in Su *et al* [20]. Briefly, the conventional approach to measuring background signal levels involves the capture of images with the laser light source blocked prior to the measurement region. However, uncontrolled laser reflections can originate anywhere along the laser path, so in particular an accurate background measurement requires that the laser actually propagate through the measurement region. We adopt a procedure in which we block only a portion of the laser sheet prior to entering the measurement region, so that the shadow of the beam block appears as a streak in the image. Since the majority of the sheet traverses the image, the resulting light level represents actual measurement conditions, and background levels can be measured accurately in the shadow of the block. The full background field is then constructed by scanning the block and its shadow across the entire image plane.

Figure 3(*a*) shows a sample background-subtracted Rayleigh scattering image, S_{RS}, with the jet present. The laser sheet enters from the right in this and all subsequent imaging windows, and each imaging window is also specified so that the side toward the laser source contains ambient fluid only. The cross-sheet signal intensity profile also shown in figure 3(*a*), compiled in the ambient region, clearly illustrates the spatial variation in laser sheet intensity. The data planes are then flat-field corrected for nonuniformity in both the camera response and the laser sheet intensity. Camera response nonuniformity can arise, for example, through lens vignetting or pixel-to-pixel variations in the imaging array itself, and can be assumed to be constant in time. Variations in the laser sheet intensity occur both in the cross-sheet direction (i.e. the vertical direction in figure 3), manifesting the spatial profile of the laser pulse itself, and in the sheet propagation direction, as a result of attenuation through scattering. The jet gas in these experiments has a similar Rayleigh scattering cross-section to that of air, so beam attenuation through the jet is assumed to be similar to attenuation in the ambient regions. The first step in the flat-field correction for camera response and sheet intensity nonuniformities accounts for these effects in the time-averaged sense, and involves dividing the jet images by time-averaged images from the same window showing Rayleigh scattering from air only (figure 3 shows a sample correction image). By using the ambient air signal for the flat-field correction, the corrected data planes are equivalent to the scattering cross-section normalized by the air value.

We next correct each image plane further for instantaneous variations in the laser sheet intensity distribution. At this stage of processing the signal levels in the ambient fluid should be identically one, so any departures from that value represent deviations of the instantaneous sheet intensity from the averaged intensity. We use the signal level profile in an arbitrary reference column from the ambient fluid region to correct the data in the remaining columns through column-by-column division, using knowledge of the laser sheet trajectory gleaned from the background measurements. Figure 3(*c*) shows the final normalized Π field, corresponding to the background-subtracted field in figure 3(*a*), fully corrected for the camera response and the instantaneous laser sheet intensity *I*.

3.3. Planar laser-induced fluorescence

3.3.1. Fluorescence imaging. In laser-induced fluorescence, the fluorescence signal intensity, S_F, in an isothermal, ideal gas mixture is given by $S_F \propto I\, X_F$, where X_F is the mole fraction of the fluorescent species, when the incident laser intensity, *I*, is much less than the saturation intensity [18]. The fluorescent

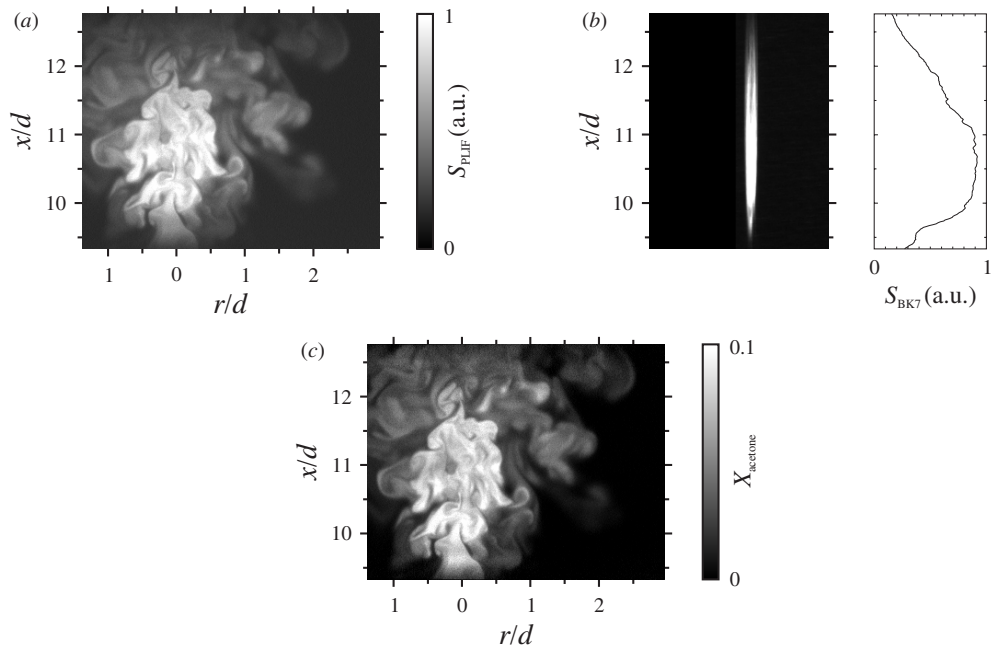

Figure 4. Data reduction for the PLIF imaging. (*a*) A sample, background-subtracted PLIF image from the $Re_\infty \approx 4600$ jet, obtained simultaneously with the scattering image in figure 3(*a*). (*b*) The simultaneous fluorescence signal from the BK7 flat used for sheet energy monitoring. (*c*) The field in (*a*) after flat-field correction, as described in section 3.3.2.

medium used in this work is acetone [5, 9, 21]. Lozano *et al* [5] confirmed the linearity of acetone fluorescence emission as a function of both incident laser intensity and acetone partial pressure, and also presented the acetone absorption and emission spectra. The absorption spectrum is primarily in the ultraviolet range, extending from 225 to 320 nm; for the current work, excitation using a frequency-quadrupled Nd:YAG laser, at 266 nm, is very near the peak in the absorption spectrum. The emission spectrum is predominantly visible, extending from 350 to 550 nm with distinct blue peaks at 445 and 480 nm, and is thus easily detected with a front-illuminated CCD camera.

Immediately before entering the flow facility, a portion of the laser sheet is directed by a fused silica flat to a BK7 glass flat for sheet intensity monitoring. One CCD camera captures the fluorescence signal from the jet flow, while a second camera simultaneously captures the fluorescence from the BK7 flat (section 3.3.2). In both cases, spectral bandpass filters (Schott BG 25) limit the 532 nm laser light that reaches the camera array while passing fluorescence emission in the blue range.

3.3.2. Data reduction: PLIF. In the data reduction for the PLIF images, we first subtract the background light levels to find the background-corrected fluorescence signal, S_F; then, we further account for both cross-sheet variations in incident laser sheet intensity, and the attenuation of the sheet as it passes through the imaging region, to determine the sheet-corrected signal, $S_{F,C}$. Finally, we scale the $S_{F,C}$ signal to obtain the acetone mole fraction X_{ac}. The measurement of background light levels is much simpler than for the Rayleigh scattering; the 266 nm laser light is only weakly detected by the camera, and the 532 nm light is largely filtered out by the bandpass filter, so conventional background measurement methods are sufficient. The cross-sheet profile of the 266 nm sheet is monitored by measuring the fluorescence signal from the BK7 glass flat, S_{BK7}, resulting in images of the form shown in figure 4(*b*). Tests confirm that the signal S_{BK7} is linear with the incident laser energy. The imaging window for the BK7 flat is referenced spatially to the PLIF imaging window in the flow itself by partially blocking the laser sheet and matching the resulting signal void regions in both images. The resulting knowledge of the sheet trajectory, together with the measured sheet intensity profile, is used to generate a tentative sheet correction image.

Attenuation of the 266 nm sheet in its propagation direction arises from both Rayleigh scattering and absorption of the light sheet. In these experiments, attenuation is accounted for in the mean only. The scattering component is estimated by measuring the Rayleigh scattering in air from a 532 nm laser sheet (as demonstrated in figure 3(*b*)). In those images, the scattering intensity attenuation in the sheet propagation direction correlates directly with the laser sheet attenuation, so we can determine directly the attenuation coefficient, α, in the Beer's law expression $I = I_0\,\mathrm{e}^{-\alpha s}$, where I is the local laser intensity, I_0 is the initial intensity (on the upstream side of the imaging window) and s is the path length. The estimated attenuation coefficient for the scattering of the 266 nm sheet is 16 times this α, reflecting the known λ^{-4} wavelength dependence of Rayleigh scattering (3.2.1). The mean absorption of the 266 nm sheet is then estimated by comparing images from simultaneous PLIF and Rayleigh scattering in a nitrogen–acetone jet, where both diagnostic methods identically provide the acetone mole fraction. With the scattering component of the attenuation correction applied to the PLIF, the remaining discrepancies in the resulting mean

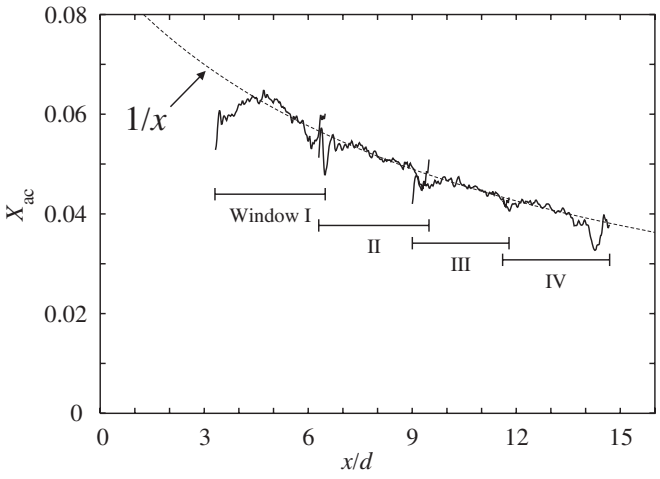

Figure 5. Mean centerline values of X_{ac} for the $Re_\infty \approx 7800$ jet, determined from the sheet-corrected PLIF signal $S_{F,C}$ after determination of the coefficient γ for each window (3). The results are consistent with the expected x^{-1} dependence found from scaling arguments [22].

fields are used to determine an absorption coefficient for the sheet attenuation. The overall mean attenuation correction is then incorporated in the final sheet correction image.

The background- and sheet-corrected PLIF signal, $S_{F,C}$, correlates directly with the acetone mole fraction, X_{ac}, in an isothermal flow, as

$$S_{F,C} = \gamma X_{ac}, \tag{3}$$

where γ is a response coefficient that is constant for a given image, but can vary between images owing to factors such as camera lens aperture, camera signal gain, laser power, etc. To calibrate the acetone fluorescence signal to obtain X_{ac}, we first acquire images from the near-nozzle region of the jet, where the unmixed potential core is present. The initial acetone mole fraction in the jet fluid, $X_{ac,0}$, is known from mass flow rate measurements (section 2.2), so γ can be determined directly for these images. For downstream imaging windows, γ is determined by enforcing continuity in the mean centerline profiles from the PLIF fields in successive windows (we ignore here the small variations in $X_{ac,0}$ arising from acetone seeding disparities). Figure 5 shows the results for the mean acetone concentration on the jet centerline for four different imaging windows in a $Re_\infty \approx 7800$ jet. The measured dependence of the mean centerline concentration on the axial coordinate, x, is consistent with the x^{-1} form expected from turbulent jet scaling arguments [22]. This represents at least a limited confirmation of the robustness of the PLIF data reduction procedure.

We note that acetone fluorescence yield in these experiments depends in principle on the relative concentrations of helium and air. However, prior results suggest that the fluorescence signal for a given acetone concentration in pure helium or pure air differs by less than 10% [21], so we neglect composition effects here. Also, acetone phosphorescence, which is known to be quenched by low concentrations of oxygen [23], might be expected to appear in the jet core, prior to acetone mixing with the ambient air. In practice, we detect no phosphorescence, which in acetone is an order of magnitude more efficient than fluorescence [24, 25], possibly owing to trace oxygen in the helium samples, dissolved air in the liquid acetone supply, or an unidentified quenching effect of the helium.

3.4. Simultaneous imaging

The simultaneous application of two laser diagnostic techniques requires a number of modifications to the experimental procedure required for the individual measurements. The measurement windows need to be registered spatially, and any instances of spectral overlap need to be measured or eliminated. The present arrangement for simultaneous Rayleigh scattering and PLIF imaging uses a beam splitter with 75% reflectance in the laser beam path. The passed beam is frequency-doubled to 266 nm, and then recombined with the reflected beam at the original 532 nm. Prior to the recombination, the reflected beam is passed through a long focal length, convex spherical lens that corrects for differences in refraction between the beams as they pass through the sheet-forming optics, ensuring that the 532 nm and 266 nm sheets both have uniform height, and that their focal points are coincident.

3.4.1. Signal cross-contamination. The long-wavelength side of the acetone fluorescence band extends up to 550 nm, which creates some signal detection issues due to spectral overlap with the 532 nm laser wavelength. With the present simultaneous imaging arrangement, it is particularly important to block stray light at 532 nm from the PLIF imaging camera, as there is significantly more light at 532 nm passing through the interrogation region as compared with a PLIF-only experiment. Here, we employ a bandpass filter (Schott BG 25, 2 mm thick) that has a peak transmittance in excess of 90% at $\approx$ 390 nm, and $<$ 1% transmittance at 532 nm. Meanwhile, imaging of the Rayleigh scattering at 532 nm is challenged by the presence of the acetone fluorescence in the visible part of the spectrum. We address this by placing a 532 nm line filter (Thorlabs FL532-10) in front of the Rayleigh scattering camera. The transmittance curve of this filter has a peak value of over 70%, and a full width at half-maximum of 10 nm.

Tests confirm that while the PLIF camera with the bandpass filter in place essentially does not detect the Rayleigh scattering at 532 nm, the Rayleigh scattering camera with the line filter does weakly detect the PLIF signal near 532 nm. To quantify this signal contamination, we perform simultaneous imaging with both cameras and their respective filters in a helium–acetone–air jet with the 266 nm light sheet only. The resulting signals thus recorded by the Rayleigh scattering and PLIF cameras can be compared, with the ratio of signal intensities representing an effective PLIF detection efficiency for the Rayleigh scattering camera. With the present arrangement, this quantity is typically around 6.5%. In the full simultaneous imaging experiments, we then map the instantaneous images from the PLIF camera, after background correction but before any sheet correction, to the Rayleigh scattering frame of reference, and subtract the predetermined fraction of this acetone fluorescence signal from the images captured by the Rayleigh scattering camera.

3.4.2. Image resolution and registration. Compared with the independent application of Rayleigh scattering or PLIF imaging, the present simultaneous imaging incurs a reduced signal-to-noise ratio (SNR), due to both lower incident laser energy, arising from the use of a single light source for both diagnostic methods, and lower detection efficiency arising from the need for optical filtration. (The uncertainty in the Rayleigh scattering measurements introduced by the correction for cross-contamination from the PLIF, discussed above, is systematic and does not have a significant effect on SNR.) The laser light allocation applied here, with 75% of the laser energy going to the Rayleigh scattering and 25% to the PLIF, was chosen through testing to minimize discrepancies in signal levels between the two diagnostic methods. As another measure to improve SNR, the imaging array pixel dimensions are reduced to 348 × 260 for the Rayleigh scattering and 325 × 257 for the PLIF, representing a 4 × 4 binning of pixels in both of the cameras. The cameras are also positioned as near as possible to the flow while maintaining a view of the full jet half-width. The Rayleigh scattering camera is fitted with an 85/f1.8 lens, while the PLIF camera is fitted with an 85/f1.2 lens (both Canon FD, 35 mm format), both operated at f1.8, to avoid resolution losses that are evident at full aperture for the f1.2 lens. With appropriate close-up lenses to allow close focusing, the resulting field of view is 30 mm (6.5 d) in the radial direction for the Rayleigh scattering (where inclusion of ambient air regions is critical (section 3.2.2)) and 22 mm (4.8 d) in the radial direction for the PLIF. The resulting pixel resolutions are 86 μm and 68 μm for the Rayleigh scattering and PLIF, respectively. The resolution of the Rayleigh scattering images is the final resolution of the mole fraction data, with the PLIF results being mapped into the imaging field of the Rayleigh scattering camera.

The spatial registration of the two imaging windows in these experiments is complicated by the need to isolate the signals captured by each camera spectrally, which means that the windows cannot easily be aligned to any common set of markers in the images. The removal of filters would potentially alter the field of view, and the use of a physical imaging target may introduce further errors due to imprecision in its positioning and alignment with respect to the laser sheet. To register the imaging regions of the two cameras at each measurement location, we perform simultaneous Rayleigh scattering and PLIF imaging in a nitrogen–acetone jet. In this flow, both images can be processed to yield the acetone mole fraction. The resulting images from the two cameras are aligned through a process that maximizes image correlations under bilinear mapping. We estimate that this process aligns the two image planes to within 0.1 pixels, or less than 9 μm, in these experiments.

3.4.3. Mole fraction calculation. Using the acetone mole fraction field, X_{ac}, measured by PLIF, the normalized signal, Π (as given by (1)), measured by Rayleigh scattering, and the mole fraction definition $1 = \sum X_i$, the mole fractions of helium and air are written as

$$X_{He} = \frac{1 - \Pi + X_{ac}\left(\frac{\sigma_{ac}}{\sigma_{air}} - 1\right)}{1 - \frac{\sigma_{He}}{\sigma_{air}}},$$

$$X_{air} = \frac{\Pi - \frac{\sigma_{He}}{\sigma_{air}} - X_{ac}\left(\frac{\sigma_{ac} - \sigma_{He}}{\sigma_{air}}\right)}{1 - \frac{\sigma_{He}}{\sigma_{air}}}. \quad (4)$$

These expressions are exact, so in principle the X_{He} and X_{air} results should be accurate provided the Π and X_{ac} results are individually accurate. However, since (4) represents an inverse problem, there are concerns that the resulting X_{He} and X_{air} will be sensitive to any uncertainties in the measured X_{ac} and Π. Uncertainties in X_{ac} and Π resulting from measurement noise would exist at fine spatial scales, so this sensitivity would likely be manifest, for example, in excessive fine structure in the X_{He} and X_{air} results, or in unphysical X_{He} and X_{air} values that lie outside the limits of 0 and 1. To confirm that these expressions are not unduly sensitive to uncertainties in X_{ac} and Π, we used the measurements described in section 4 to compare the X_{He} and X_{air} determined both through the direct application of (4), and through an optimization process that enforces consistency with both (4) and a smoothness condition on the resulting X_{He} field.

The optimization proceeds by defining a functional, $E = E_1 + \beta E_2$, where E_1 is itself defined as

$$E_1 \equiv \left[\Pi + X_{ac}\left(1 - \frac{\sigma_{ac}}{\sigma_{air}}\right) + X_{He}\left(1 - \frac{\sigma_{He}}{\sigma_{air}}\right) - 1\right]^2, \quad (5)$$

so that $E_1 = 0$ when the solution for X_{He}, and the measured Π and X_{ac}, satisfy (1) exactly; E_2, which serves as a regularization condition [26], is defined as

$$E_2 \equiv \nabla X_{He} \cdot \nabla X_{He}, \quad (6)$$

and thus assumes small values when the X_{He} solution is smooth. The arbitrary coefficient β in the E definition allows us to vary the relative importance of the smoothness condition E_2. We solve for X_{He} by minimizing the (discrete) integral of E over the measurement domain using the tools of variational calculus. The normal gradient of X_{He} is set to zero at the boundaries of the domain. Then, we determine X_{air} from X_{ac}, X_{He} and the definition of the mole fraction.

Applying this optimization process to the present data, we find that the results for X_{He} and X_{air} are largely independent of β over the range $\beta = 0$ (i.e. direct solution of (4)) to $\beta = 0.25$. That is, X_{He} and X_{air} only minimally manifest any unphysical magnitudes or fine structure regardless of the enforced smoothness level, indicating that (4) is not in fact particularly sensitive to measurement uncertainty. This sensitivity is also explored from a different perspective in section 4.2 below. (Details of the solution comparison for different β are given in [17].) The results presented in this paper are thus determined through direct solution of (4), with no additional smoothness constraint.

Given the particular parameters of the present experiments, it is not surprising that the determination of X_{He} and X_{air} requires no smoothness constraint. In both the X_{He} and X_{air} expressions in (4), the problematic term is the relatively large coefficient of the X_{ac} term, namely $\sigma_{ac}/\sigma_{air} - 1 \approx 13$ in the X_{He} expression and $(\sigma_{ac} - \sigma_{He})/\sigma_{air} \approx 14$ in the X_{air} expression, which potentially exaggerates the effect of errors in the measured X_{ac}. In particular, if we denote the

Table 1. Run conditions and window parameters for the imaging experiments. The jet Reynolds number Re_∞ is defined using the kinematic viscosity of the ambient air, while Re_0 is defined using the kinematic viscosity of the jet gas mixture. Successive window locations are labeled I through IV. The initial helium and acetone mole fractions in each case are $X_{\mathrm{He},0}$ and $X_{\mathrm{ac},0}$, and u_0 is the jet exit bulk velocity. For each measurement window, $x_{\min}$ and $x_{\max}$ are the upstream and downstream limits of the window, while r_L and r_R are the maximum radial displacements of each window on either side of the jet centerline.

Case	Re_∞ (Re_0)	Window	$X_{\mathrm{He},0}$:$X_{\mathrm{ac},0}$	u_0	$(x_{\min}, x_{\max})$	(r_L, r_R)
Low *Re*	4630 (1800)	I	0.901:0.099	15.6 m s^{-1}	(5.7*d*, 8.7*d*)	(1.8*d*, 2.7*d*)
	4540 (1510)	II	0.920:0.080	15.3 m s^{-1}	(9.7*d*, 12.4*d*)	(1.3*d*, 3.0*d*)
High *Re*	7810 (2260)	I	0.935:0.065	26.3 m s^{-1}	(3.1*d*, 6.6*d*)	(2.3*d*, 2.6*d*)
	7830 (2400)	II	0.929:0.071	26.4 m s^{-1}	(6.1*d*, 9.6*d*)	(1.6*d*, 3.2*d*)
	7810 (2280)	III	0.934:0.066	26.3 m s^{-1}	(8.8*d*, 11.9*d*)	(0.7*d*, 4.1*d*)
	7780 (2180)	IV	0.938:0.062	26.2 m s^{-1}	(11.4*d*, 14.8*d*)	(0.8*d*, 4.0*d*)

uncertainty or error in a given quantity by δ_i, then, by standard uncertainty analysis, we can write δ_{He} as

$$\delta_{\mathrm{He}} \approx \left[\delta_\Pi^2 + (13\,\delta_{\mathrm{ac}})^2\right]^{1/2}. \tag{7}$$

However, this effect is mitigated here by the relatively low acetone concentrations, recognizing that (7) describes absolute, as opposed to relative, errors. If we define signal-to-noise ratios (SNR) in a general sense as $\mathrm{SNR}_{\mathrm{He}} \equiv X_{\mathrm{He,ref}}/\delta_{\mathrm{He}}$, $\mathrm{SNR}_{\mathrm{ac}} \equiv X_{\mathrm{ac,ref}}/\delta_{\mathrm{ac}}$, and $\mathrm{SNR}_\Pi \equiv \Pi_{\mathrm{ref}}/\delta_\Pi$, where $X_{\mathrm{He,ref}}$, $X_{\mathrm{ac,ref}}$ and Π_{ref} are reference values, then (7) can be recast in terms of relative errors as

$$\mathrm{SNR}_{\mathrm{He}} = \left[\left(\frac{\Pi_{\mathrm{ref}}}{X_{\mathrm{He,ref}}}\right)^2 \frac{1}{\mathrm{SNR}_\Pi^2} + \left(\frac{13\,X_{\mathrm{ac,ref}}}{X_{\mathrm{He,ref}}}\right)^2 \frac{1}{\mathrm{SNR}_{\mathrm{He}}^2}\right]^{-1/2}. \tag{8}$$

As noted in section 4.1, X_{ac} in the jet mixture is relatively low, at no higher than 0.099, in the present experiments; in (8), this counters the tendency of the coefficient $\sigma_{\mathrm{ac}}/\sigma_{\mathrm{air}} - 1 \approx 13$ to reduce $\mathrm{SNR}_{\mathrm{He}}$. The measured values of these SNR for the present experiments are discussed in section 4.2.

4. Results and analyses

4.1. Run conditions

We consider two jet flow cases here, with the experimental conditions as given in table 1. The first is at a relatively low Reynolds number ($Re_\infty \approx 4600$, where Re_∞ is the jet exit Reynolds number based on the nozzle diameter, $d = 4.6$ mm, the jet exit bulk velocity, u_0, and the kinematic viscosity of the ambient air, $\nu_{\mathrm{air}} = 1.55 \times 10^{-5}$ m^{2}s^{-1}), while the second is at $Re_\infty \approx 7800$. The use of Re_∞ to characterize the flow reflects that as the jet moves downstream, the jet fluid is dominated by the entrained air [27]. All data windows are cropped in the radial direction to include only those regions that are covered by both the PLIF and the Rayleigh scattering imaging cameras, and are further cropped in the axial direction to include only regions that have adequate laser illumination for both the Rayleigh scattering and PLIF, where the degree of illumination is assessed from cross-sheet laser intensity profiles such as those shown in figures 3(*a*) and 4(*b*). At the lower Reynolds number, the two imaging windows span respectively from $x/d = 5.7$ to $x/d = 8.7$ and from $x/d = 9.7$ to $x/d = 12.4$ in the axial direction. For the higher Reynolds number case, four imaging windows span collectively from $x/d = 3.1$ to $x/d = 14.8$. The raw imaging windows are sized as specified in section 3.4.2, so the final pixel resolution of the data fields is $\Delta x = 86\,\mu$m.

In all cases, the initial helium:acetone ratio is chosen to be relatively near the ratio 0.938:0.062 for which the mixture will have the same Rayleigh scattering cross-section as air. This is the approach taken with Rayleigh scattering-only studies of differential diffusion using two jet species [13, 14, 28], where the normalized scattering signal is $\Pi = 1$ unless the jet species deviate from their initial proportions. Thus, while the Rayleigh scattering results in this work alone provide a similar, specific level of insight into the differential diffusion process as those earlier studies, the full mole fraction information provided by the addition of the acetone PLIF gives a more complete picture of the full multi-species mixing process. The slight differences in both the ratio $X_{\mathrm{He},0}:X_{\mathrm{ac},0}$ and u_0 for the different experimental runs owe to variations in the acetone flow rate that are primarily due to ambient temperature changes. For the lower Reynolds number case, the helium mole fractions were $X_{\mathrm{He},0} = 0.901$ and 0.920 in the two imaging windows, and the jet bulk velocities were $u_0 = 15.6$ and 15.3 m s^{-1}. For the higher Reynolds number case, $X_{\mathrm{He},0}$ ranged from 0.929 to 0.938, and u_0 ranged from 26.2 to 26.4 m s^{-1}.

The flow conditions at the jet exit are appropriately described by Re_0, the Reynolds number based on d, u_0, and ν_m, the kinematic viscosity of the jet mixture. The value of ν_m is found for each case using the dynamic viscosities of helium and acetone vapor, $\mu_{\mathrm{He}} = 2.0 \times 10^{-5}$ kg m^{-1}s^{-1} and $\mu_{\mathrm{ac}} = 0.76 \times 10^{-5}$ kg m^{-1}s^{-1}, and the mixture dynamic viscosity formula in [29], and the densities $\rho_{\mathrm{He}} = 0.164$ kg m^{-3} and $\rho_{\mathrm{ac}} = 2.38$ kg m^{-3}. For the lower Reynolds number case, the Re_0 values (1800 and 1510 for the two imaging windows) are below the value of $Re_0 \approx 2300$ at which we expect the onset of the turbulent transition in a pipe flow, and we observe that the jet flow in that case is initially laminar, and generally undergoes the turbulent transition somewhere in the middle of the upstream imaging window. The extended laminar region of the low *Re* case, and, in particular, the smooth mole fraction fields that result, are well suited for basic assessment of the present mole fraction measurement method. In contrast, the higher *Re* case, for which the Re_0 values are near the pipe flow transition value, is essentially turbulent throughout, so the results will be more reflective of practical studies of multicomponent effects in turbulent mixing.

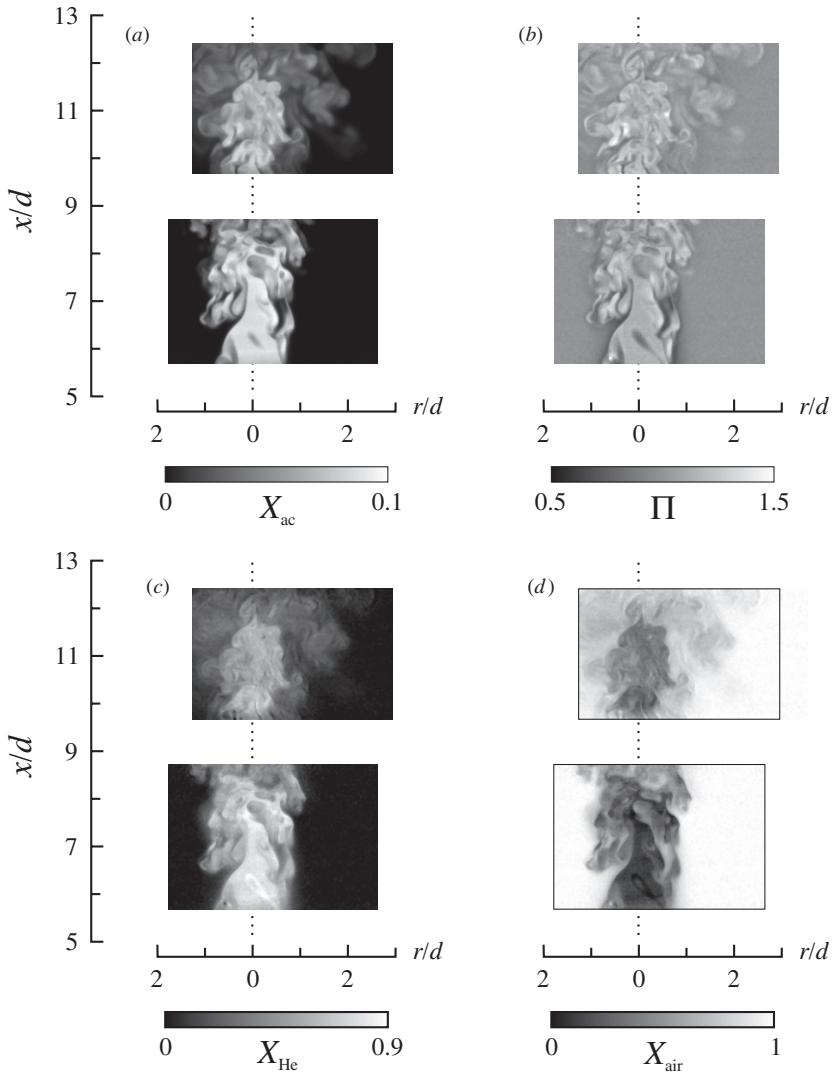

Figure 6. Results from the simultaneous Rayleigh scattering and PLIF imaging in a jet with jet exit Reynolds number $Re_\infty \approx 4600$. (*a*) The acetone mole fraction field, X_{ac}, measured by PLIF, (*b*) the normalized Rayleigh scattering field Π, (*c*) the helium mole fraction field X_{He} and (*d*) the air mole fraction field X_{air} determined using (4). For this relatively low Reynolds number, the turbulent transition is typically near the center of the upstream image.

4.2. Sample results

Figure 6 gives sample images and computed mole fraction fields from the $Re_\infty \approx 4600$ case, while figure 7 gives sample results for the $Re_\infty \approx 7800$ case. The figures show the acetone mole fraction fields, X_{ac}, determined directly from the PLIF images, the normalized Rayleigh scattering signals, Π, and the helium and air mole fraction fields, X_{He} and X_{air}, determined using (4). All fields shown have been filtered with a 3×3 median filter, post-processing, to reduce noise at a minimal cost to image resolution [30]. We estimate the camera noise in the (unfiltered) X_{ac} fields by comparing the standard deviation of X_{ac} in the ambient region with the reference X_{ac} from the jet core, giving an SNR of 330; the standard deviation of X_{ac} in the jet core, arising from camera noise and the peak shot noise, compared with the core X_{ac} gives $\mathrm{SNR}_{ac} = 33$. For the unfiltered Π fields, where the signal levels are comparatively tightly distributed around the ambient values, a comparison of the standard deviation of Π in the ambient region, which reflects both camera and shot noise, with the mean signal level there gives $\mathrm{SNR}_\Pi = 49$.

We can also quantify in a similar fashion the 'noise' (or, more precisely, solution uncertainty) in the unfiltered helium mole fraction fields determined from (4). In the jet potential core, the comparison of the standard deviation of X_{He} with its mean value gives $\mathrm{SNR}_{He} = 22$. In the ambient region, the standard deviation of X_{He} compared with the core X_{He} gives $\mathrm{SNR}_{He} = 27$. These SNR are only slightly lower than those for the raw X_{ac} and Π measurements, confirming that there is only a small increase in uncertainty introduced by the direct solution of (4). In fact, inserting the values $\mathrm{SNR}_{ac} = 33$ and $\mathrm{SNR}_\Pi = 49$ measured in the jet core in expression (8), we find $\mathrm{SNR}_{He} = 20$ for $X_{He,0} = 0.901$, and $\mathrm{SNR}_{He} = 29$ for $X_{He,0} = 0.938$, which is fully consistent with the values $\mathrm{SNR}_{He} = 22$ and 27 reported here for the different definitions of the X_{He} noise.

Consistent with earlier studies [13, 14], the Π fields show that differential diffusion is present across the radial extent of

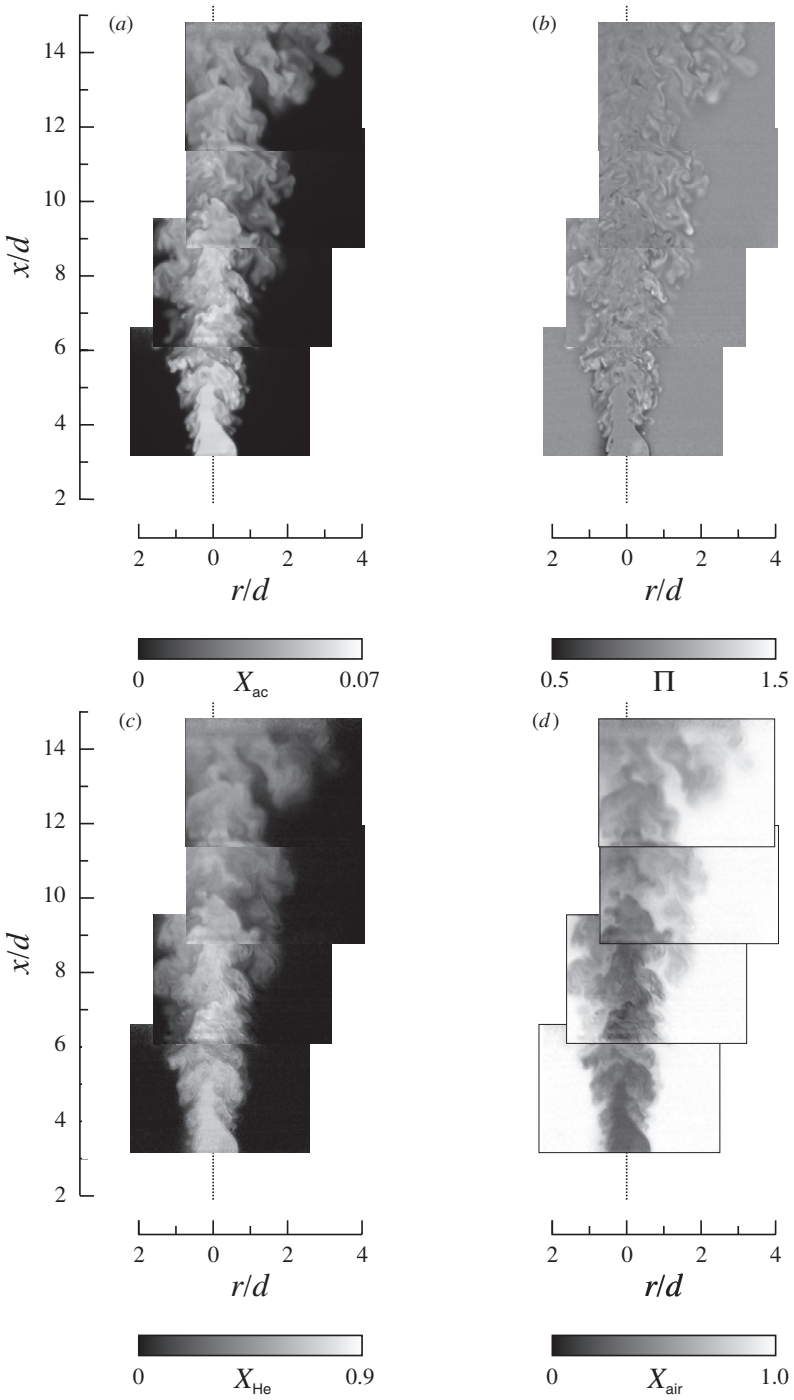

Figure 7. Results from simultaneous Rayleigh scattering and PLIF imaging in a jet with $Re_\infty \approx 7800$. (*a*) The acetone mole fraction field, X_{ac}, measured by PLIF, (*b*) the normalized Rayleigh scattering field Π, (*c*) the helium mole fraction field X_{He} and (*d*) the air mole fraction field X_{air} determined using (4).

the turbulent regions of the flow, even though, in the near field, it only arises at the jet boundary, where the three species are in proximity. The similarity between the helium and acetone mole fraction fields is clear, and not surprising considering their identical, uniform distribution in the jet fluid. The mole fraction fields are in other ways qualitatively similar to expectations. The X_{He} field is visibly smoother than the X_{ac} field, corresponding to the higher molecular diffusivity of helium as compared to acetone. The X_{air} field is particularly interesting when examined alongside the normalized Rayleigh scattering signal Π. For example, regions in the Π field where $\Pi = 1$ can represent pure air, or any mixture of air, helium and acetone where the helium and acetone mole fractions are given by $X_{He}\sigma_{He} + X_{ac}\sigma_{ac} = (X_{He} + X_{ac})\sigma_{air}$. The additional information provided by X_{air} allows us to differentiate between these mixing states. An example of this is in the most downstream window in figure 7(*d*), which shows a significant pocket of air that has been engulfed into

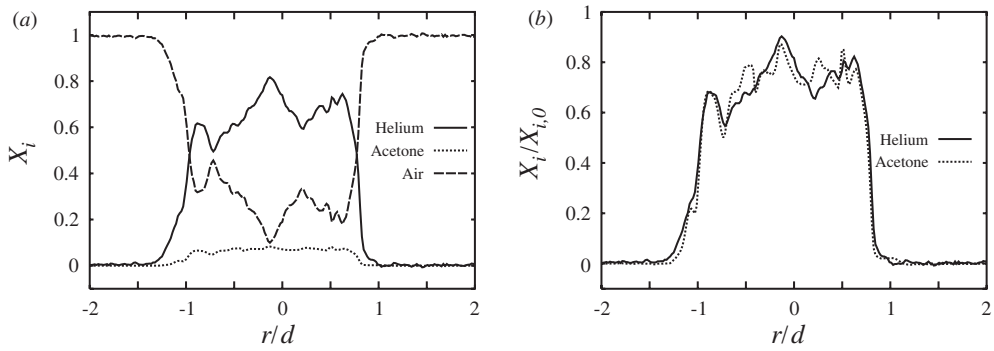

Figure 8. (*a*) Mole fraction profiles from the $Re_\infty \approx 4600$ jet of figure 6, at $x/d = 7.5$. (*b*) The profiles from (*a*), normalized by the initial mole fraction values $X_{i,0}$ at the jet exit. The effects of differential diffusion from the laminar portion of the jet are clear.

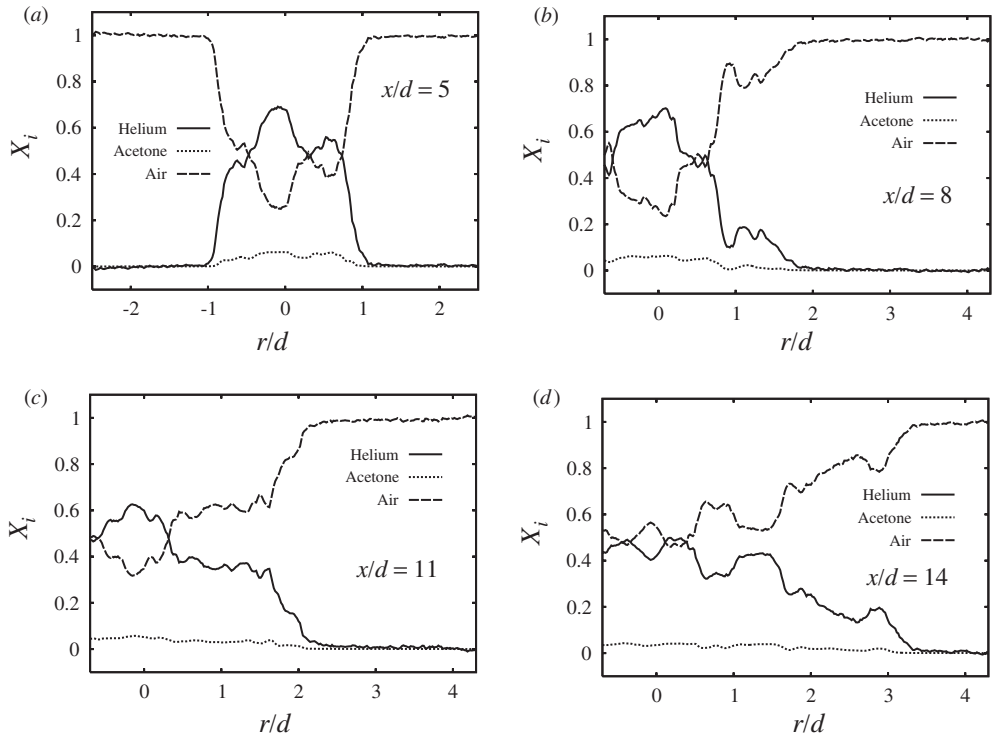

Figure 9. Mole fraction profiles from the $Re_\infty \approx 7800$ jet of figure 7. Profiles are compiled at (*a*) $x/d = 5$, (*b*) $x/d = 8$, (*c*) $x/d = 11$ and (*d*) $x/d = 14$.

the jet. From the normalized scattering signal in figure 7(*b*) alone, it is unclear whether this region represents entrained air, or negligible differential diffusion of the initial jet fluid for which the scattering cross-section is close to the air value.

4.3. Instantaneous mole fraction fields

With the present data for the individual mole fractions, one way to examine the effect of disparate molecular diffusivities on the mixing is to compare radial profiles from each of the mole fraction fields. The analyses in this section are indicative of the additional insight afforded by the individual mole fractions, compared with the variable Π only as measured in earlier studies [13, 14]. Figure 8(*a*) shows instantaneous profiles, from $x/d = 7.5$, of the mole fractions of all three gases from the $Re_\infty \approx 4600$ case, from the upstream data plane in figure 6. Figure 8(*b*) shows the same X_{He} and X_{ac} profiles, but normalized by the initial mole fraction values at the jet exit to facilitate comparison. Figure 9 shows instantaneous mole fraction profiles from $x/d = 5$, 8, 11, and 14 for the high Reynolds number data in figure 7. Figure 10 shows the X_{He} and X_{ac} profiles from figure 9 normalized by the mole fraction values at the jet exit, together with the profiles of the normalized scattering signal Π at the same downstream locations. The normalized X_{He} and X_{ac} profiles show clearly that the helium mole fraction field is smoother, and slightly (though noticeably) wider in the near-nozzle region. Both of these properties are expected given that the helium:air molecular diffusivity is higher than the acetone:air diffusivity.

There is a clear correlation between the profiles of X_{ac} and Π shown in figure 10 even at the small scales. This

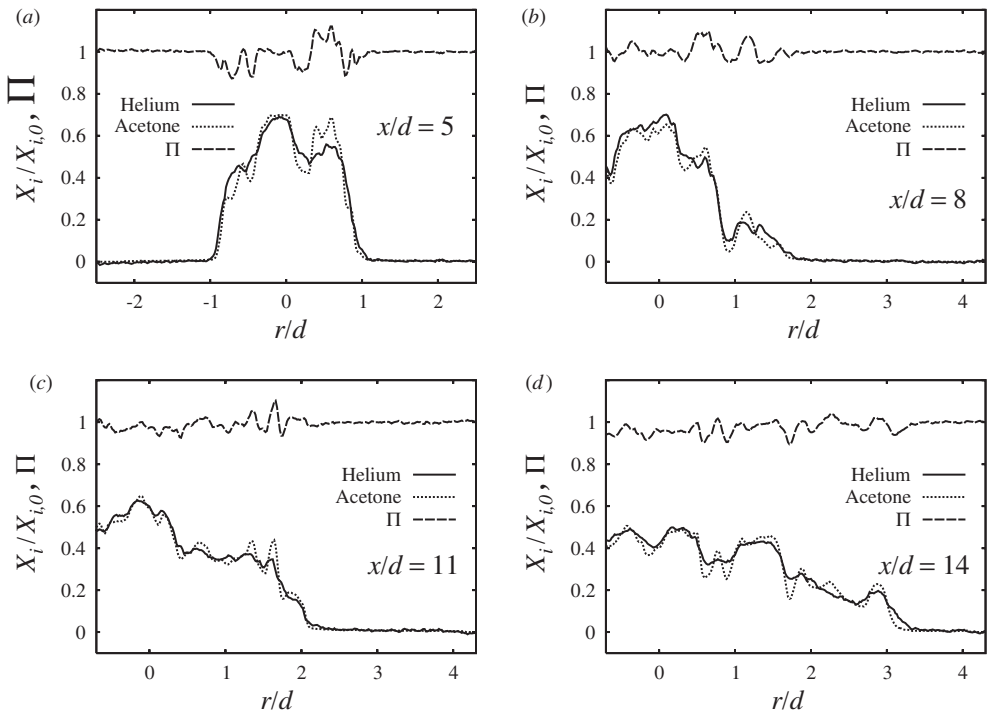

Figure 10. The profiles of X_{He} and X_{ac} from figure 9, normalized by their values at the jet exit, along with profiles of the normalized scattering signal Π. Profiles are compiled at (*a*) $x/d = 5$, (*b*) $x/d = 8$, (*c*) $x/d = 11$ and (*d*) $x/d = 14$. The general similarity between the X_{He} and X_{ac} profiles is clear, as is the correlation between the fine-scale features in the X_{He} and Π profiles.

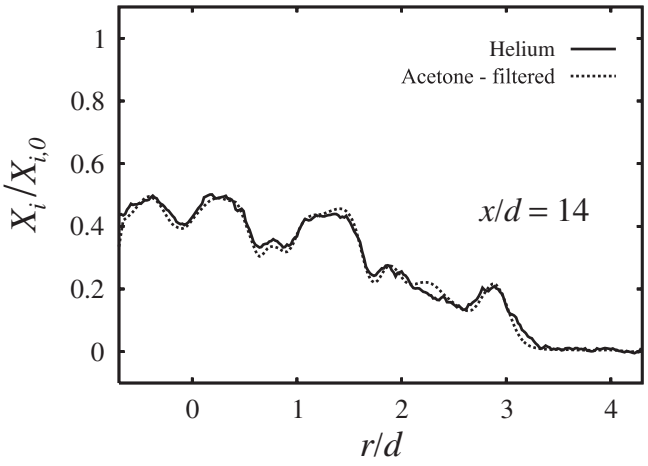

Figure 11. Comparison of the X_{He} profile from figure 10(*d*) with the corresponding X_{ac} profile after filtering with an 11 × 11 pixel ($0.2\,d \times 0.2\,d$) top-hat filter. The similarity between these profiles, compared to the profiles in the previous figure, is illustrative of the impact differential diffusion has on small flow scales.

positive correlation yields the relatively smooth helium mole fraction field by the nature of (4). There is also a strong correlation between the helium mole fraction field and the spatially filtered acetone mole fraction field, when the filter size is significant compared to the smallest eddies in the flow. This is evident in figure 11, which shows again the normalized profile of X_{He} at $x/d = 14$ in the $Re_\infty \approx 7800$ jet (from figure 9(*d*)), as well as the corresponding profile of X_{ac} after application of an 11 × 11 pixel ($0.2\,d \times 0.2\,d$) top-hat filter. The similarity of these profiles implies that the differences between the mole fraction fields of the less- and more-diffusive scalars is primarily in the high-wavenumber range, in this developing region of the flow. This then suggests that, in this part of the flow, unmixing of the jet species by differential diffusion is significant relative to inertial separation mechanisms, whereby species with different densities respond differently to, for example, buoyancy effects or centripetal acceleration in swirling motions. While differential diffusion acts initially at the small scales, inertial separation would be more evident with larger fluid volumes.

Another way to interpret the results shown in figure 10 is that individual structures in the X_{He} field (which will take the form of dissipation layers [2]) generally align with those in the X_{ac} field, and that the fields differ primarily in the thickness of those structures, with the helium mole fraction fields showing thicker structures as a result of the higher diffusivity of helium. This observation has direct relevance to computational approaches to multi-species mixing. Models that represent the scalar evolution using the single mixture fraction variable would potentially be able to handle multiple scalar fields whose structures were aligned by using scaling factors to account for different structure thicknesses; however, models would be particularly challenged if the structures in the different scalar fields were not aligned. The utility of these individual mole fraction measurements is evident when we note that earlier studies of differential diffusion [13, 14] that provide only measurements of Π can only identify the presence of unmixing of the multiple species, and would be unable to discriminate conclusively between the cases in which the scalar structures were or were not aligned.

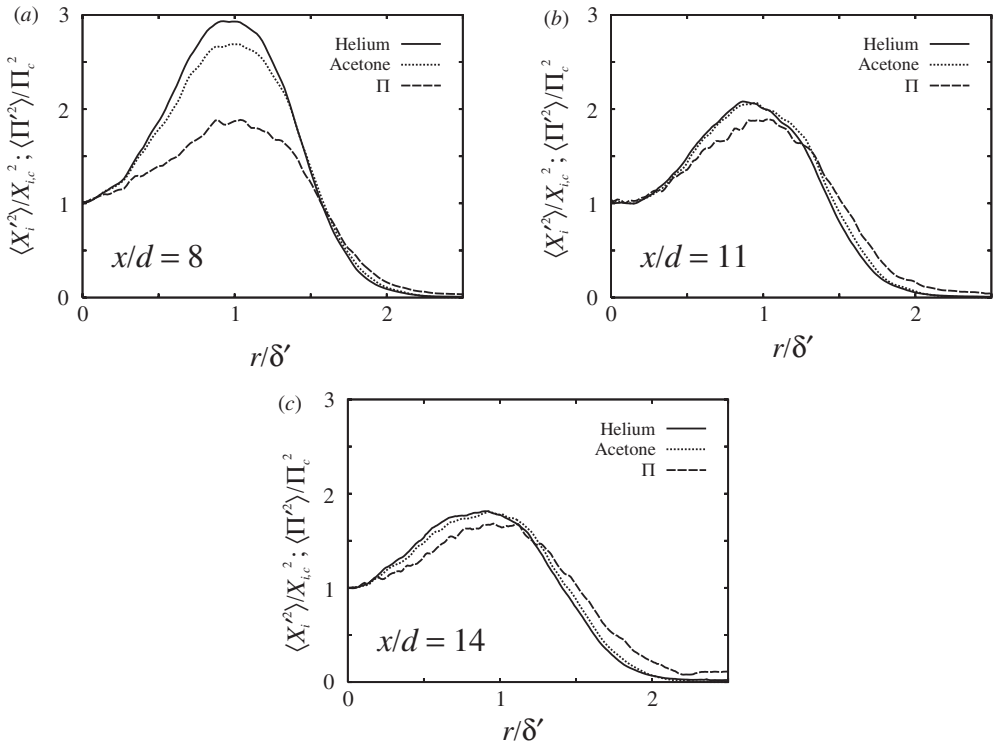

Figure 12. Similarity profiles of the normalized variance of X_{He}, X_{ac} and Π for the $Re_\infty \approx 7800$ jet at (*a*) $x/d = 8$, (*b*) $x/d = 11$ and (*c*) $x/d = 14$. The similarity length δ' is defined as the radial position of maximum variance in the Π field.

Figure 12 shows profiles of the variances of X_{He}, X_{ac} and Π from the $Re_\infty \approx 7800$ jet, each normalized by its centerline value and expressed in terms of the similarity coordinate r/δ', where $r = \delta'$ is the location of maximum variance in the Π profile. In the relatively near field ($x/d = 8$, figure 12(*a*)), the peak-normalized helium mole fraction fluctuations are notably larger than the peak acetone mole fraction fluctuations. Since X_{He} and X_{ac} have the same initial conditions, differences in their fluctuations must arise from differential diffusion; it is likely that the stronger tendency for helium to diffuse radially outward means that helium is introduced first into the turbulent shear layer on the edges of the flow, so that the near-field X_{He} fluctuations are larger than X_{ac} fluctuations, as seen in figure 12(*a*). For $x/d = 11$ and 14 (figures 12(*b*) and (*c*)), the acetone and helium mole fraction fluctuation profiles collapse to a similar form (in fact, the X_{ac} profile is very slightly wider) as the flow approaches its asymptotic turbulent state, where transport effects should become negligible. Figure 12 also shows that the fluctuation profiles of the normalized scattering signal, Π, are consistently wider than the profiles of both X_{He} and X_{ac}. Deviations of Π from its mean require deviations of either X_{He} or X_{ac}, or both, from their respective means; for the Π fluctuation profile to be wider than both mole fraction fluctuation profiles suggests that as the turbulent flow develops, there is no strong bias toward either fluid at the far edges of the jet, as neither helium nor acetone alone can be readily identified as being responsible for significant Π fluctuation events.

5. Conclusions

We have demonstrated a technique for performing quantitative planar measurements of multiple species mole fractions in a turbulent flow. The flow system studied is an axisymmetric jet, where the jet fluid is a mixture of helium and acetone, issuing into co-flowing air. The method employs simultaneous PLIF and planar Rayleigh scattering. The PLIF measures the concentration of acetone, while the Rayleigh scattering provides a measure of the acetone–helium relationship. The experimental protocol emphasizes the quantitative accuracy of the individual imaging measurements. An inversion process then determines the individual mole fractions from the PLIF and Rayleigh scattering measurement results.

Results using this method are able to show subtle differences in the concentration fields of the two jet species, where differential mixing occurs due to their disparate diffusive properties. Prior work in multi-species jets at moderately turbulent Reynolds numbers [13] has shown that differential diffusion is persistent over a range of Re and may be particularly important in reacting flows, where heat release can lead to significant local flow laminarization. The present method can augment our understanding of these multicomponent mixing phenomena and can assist efforts to simulate these systems, by allowing detailed investigation of quantities such as dissipation or energy spectra for the individual scalars. The method can also be adapted to different diffusivity or Schmidt number ratios in the gaseous jet species; acetone could be replaced by other fluorescent tracers, and helium by other species, provided that the jet species and air maintain distinct scattering cross-sections.

Acknowledgments

This work is supported by the National Science Foundation through grant CBET-0348208.

References

[1] Escoda M C and Long M B 1983 Rayleigh scattering measurements of the gas concentration field in turbulent jets *AIAA J.* **21** 81–4
[2] Buch K A and Dahm W J A 1998 Experimental study of the fine-scale structure of conserved scalar mixing in turbulent shear flows: part 2. $Sc \approx 1$ *J. Fluid Mech.* **364** 1–29
[3] Miles R B, Lempert W R and Forkey J N 2001 Laser Rayleigh scattering *Meas. Sci. Technol.* **12** 33–51
[4] Su L K and Clemens N T 2003 The structure of fine-scale scalar mixing in gas-phase turbulent jets *J. Fluid Mech.* **488** 1–29
[5] Lozano A, Yip B and Hanson R K 1992 Acetone: a tracer for concentration measurements in gaseous flows by planar laser-induced fluorescence *Exp. Fluids* **13** 369–76
[6] McDonell V G and Samuelsen G S 2000 Measurement of fuel mixing and transport processes in gas turbine combustion *Meas. Sci. Technol.* **11** 870–86
[7] Su L K, Han D H and Mungal M G 2000 Measurements of velocity and fuel concentration in the stabilization region of lifted jet diffusion flames *Proc. Combust. Inst.* **28** 327–34
[8] VanCruyningen I, Lozano A and Hanson R K 1990 Quantitative imaging of concentration by planar laser-induced fluorescence *Exp. Fluids* **10** 41–9
[9] Thurber M C and Hanson R K 2001 Simultaneous imaging of temperature and mole fraction using acetone planar laser-induced fluorescence *Exp. Fluids* **30** 93–101
[10] Hassel E P and Linow S 2000 Laser diagnostics for studies of turbulent combustion *Meas. Sci. Technol.* **11** 37–57
[11] Frank J H, Kaiser S A and Long M B 2005 Multiscalar imaging in partially premixed jet flames with argon dilution *Combust. Flame* **143** 507–23
[12] Dibble R W and Long M B 2005 Investigation of differential diffusion in turbulent jet flows using planar Rayleigh scattering *Combust. Flame* **143** 644–9
[13] Brownell C J and Su L K 2008 Planar laser imaging of differential molecular diffusion in gas-phase turbulent jets *Phys. Fluids* **20** 035109
[14] Cozzi F, Olivani A, Caratti L and Coghe A 2010 Investigation of fine scale structure of turbulent and molecular diffusion in coaxial jets of He/CO_2 in air by LDA and Rayleigh scattering *Exp. Therm. Fluid Sci.* **34** 316–22
[15] Bartels J *et al* 1962 *Landolt–Bornstein Numerical Data and Functional Relationships in Science and Technology* 6th edn (Berlin: Springer)
[16] Ambrose D, Sprake C H S and Townsend R 1974 Thermodynamic properties of organic oxygen compounds XXXIII. The vapour pressure of acetone *J. Chem. Thermodyn.* **6** 693–700
[17] Brownell C J 2008 Quantitative imaging of multi-species fluid mixing in turbulent flows *PhD Thesis* Johns Hopkins University, Baltimore, MD
[18] Eckbreth A 1988 *Laser Diagnostics for Combustion Temperature and Species* (Kent: Abacus Press)
[19] Bilger R W and Dibble R W 1982 Differential diffusion effects in turbulent mixing *Combust. Sci. Technol.* **28** 161–72
[20] Su L K, Helmer D B and Brownell C J 2010 Quantitative planar imaging of turbulent buoyant jet mixing *J. Fluid Mech.* **643** 59–95
[21] Thurber M C and Hanson R K 1999 Pressure and composition dependencies of acetone laser-induced fluorescence with excitation at 248, 266 and 308 nm *Appl. Phys.* B **69** 229–40
[22] Chen C J and Rodi W 1980 *Vertical Turbulent Buoyant Jets: A Review of Experimental Data* (Oxford: Pergamon)
[23] Groh H J, Luckey G W and Noyes W A 1950 The mechanism of acetone vapor fluorescence *J. Chem. Phys.* **21** 115–8
[24] Heicklen J 1959 The fluorescence and phosphorescence of biacetyl vapor and acetone vapor *J. Am. Chem. Soc.* **81** 3863–6
[25] Gandini A and Kutschke K O 1968 The primary process in the photolysis of hexafluoroacetone vapour: II. The fluorescence and phosphorescence *Proc. R. Soc.* A **306** 511–28
[26] Tikhonov A N and Arsenin V Y 1977 *Solutions of Ill-Posed Problems* (New York: Wiley)
[27] Ricou F P and Spalding D B 1961 Measurements of entrainment by axisymmetrical turbulent jets *J. Fluid Mech.* **11** 21–32
[28] Kerstein A R, Dibble R W, Long M B, Yip B and Lyons K M 1989 Measurement and computation of differential molecular diffusion in a turbulent jet *Proc. 7th Symp. Turb. Shear Flows* pp 14.2.1–14.2.5
[29] Bird R B, Stewart W E and Lightfoot E N 1960 *Transport Phenomena* (New York: Wiley)
[30] Ghandhi J B 2006 Spatial resolution and noise considerations in determining scalar dissipation rate from passive scalar image data *Exp. Fluids* **40** 577–88